Chinese Journal of Chemical Engineering 89 (2026) 145–156

Contents lists available at ScienceDirect

Chinese Journal of Chemical Engineering

journal homepage: www.elsevier.com/locate/CJChE

Full Length Article

Numerical simulation of multicomponent hydrocarbon flow and heat transfer in a regenerative catalytic oxidizer

Yujie Kang [1], Guangrun Yang [1], Jingxiao Wang [1], Zhongjie Shen [1], Jianliang Xu [1,*], Zhenghua Dai [1], Haifeng Liu [1,2,*]

[1] National Energy Coal Gasification Technology Research and Development Center and Shanghai Engineering Research Center of Coal Gasification, East China University of Science and Technology, Shanghai 200237, China
[2] Liaoning Petrochemical University, Fushun 113001, China

ARTICLE INFO

Article history:
Received 7 April 2025
Received in revised form
13 August 2025
Accepted 15 August 2025
Available online 9 October 2025

Keywords:
Volatile organic compounds
Regenerative catalytic oxidizer
Catalysis
Numerical simulation
Alkane
Heat transfer

ABSTRACT

Regenerative catalytic oxidizers (RCO) are widely used to remove volatile organic compounds (VOCs) due to their energy-saving and stability. In this study, a multi-component catalytic reaction model was constructed to numerically investigate the reaction process of hydrocarbon-containing VOCs in RCO using computational fluid dynamics (CFD) simulation. To obtain the conversion characteristics of multi-component hydrocarbons, the effects of intake load, equivalence ratio, and the composition of multi-component hydrocarbons on the flow, heat transfer, and conversion rate of the reactor were analyzed. A feasibility study plan targeting the hard-to-convert components was also proposed. The results indicated that as the load increases, the conversion rates of the various components decrease, while the reaction rates increase. Moreover, increasing the flow velocity intensifies turbulence and enhances the collision frequency between the gas and the wall surfaces. This, in turn, amplifies the resistance effect of the porous medium. As the equivalence ratio of VOCs to oxygen increases, the oxygen-deficient condition leads to a decrease in the molecular weight of the hydrocarbons involved in the reaction. The reaction temperature also shows a downward trend. A comparative analysis of the catalytic combustion characteristics of multi-component VOCs and single-component gases reveals that adding ethane and propane can facilitate methane oxidation.

1. Introduction

Coal remains the dominant energy source in China. According to the National Bureau of Statistics, China's total energy consumption reached 59.6 billion tons of standard coal in 2024, with coal accounting for 53.2% of this total [1]. Coal conversion processes aim to maximize the dual benefits of coal as both an energy resource and a chemical feedstock. However, these processes also lead to significant emissions of low-concentration VOCs, posing an urgent environmental challenge. VOCs are pollutants that have substantial impacts on the environment, human health, and the survival of plants and animals. They participate in atmospheric photochemical reactions, contributing to the formation of ozone and $PM_{2.5}$. Furthermore, exposure to VOCs can directly harm human health by causing respiratory, neurological, and other adverse effects [2,3]. Given these multifaceted impacts, it is essential to conduct in-depth research on efficient VOCs treatment technologies.

Regenerative catalytic oxidation (RCO) is a highly energy-efficient and effective technology for the removal of VOCs. It operates on a principle similar to that of regenerative thermal oxidation (RTO), but with a lower reaction temperature, which rarely causes secondary pollution [4–7]. The honeycomb monoliths are characterized by a higher specific surface area and lower pressure drop. They are also easy to recycle and cost-effective [8]. These characteristics have led to the widespread application of honeycomb monoliths in current RCO systems. In these systems, they serve dual functions as both heat storage/release media and catalyst supports [9]. However, the dense porous structures within RCO make it challenging to directly measure many critical parameters. CFD can efficiently address the coupled multiphysics problems within these oxidizers, significantly reducing experimental costs. As a result, CFD has become a primary method for studying the internal flow and heat transfer processes in RCO.

* Corresponding authors.
E-mail addresses: xujl@ecust.edu.cn (J. Xu), hfliu@ecust.edu.cn (H. Liu).

https://doi.org/10.1016/j.cjche.2025.08.016

Operating conditions are critical factors influencing the treatment efficiency of VOCs. Numerous studies have examined the impacts of inlet velocity, concentration, and switching time on combustion efficiency [10–12]. Additionally, several studies based on single-channel systems have investigated heat exchange and VOC conversion within heat accumulator channels [13–16]. However, it is important to note that the aforementioned studies all used single-component hydrocarbons as surrogates for VOCs. In contrast, waste gases in actual industrial processes are highly complex in composition. Experimental findings have shown that during combustion reactions, specific hydrocarbon mixtures exhibit mutual promotion or inhibition due to competitive adsorption [17,18]. For example, Xia *et al.* [19] conducted an in-depth study on the catalytic activity of toluene/xylene, acetone/ethyl acetate, acetone/xylene, and ethyl acetate/xylene mixtures. Their results indicated that competitive adsorption of these typical VOCs on the catalyst surface inhibits their oxidation. Similarly, He *et al.* [20] found that in the catalytic oxidation of multi-component VOCs, benzene and toluene inhibit the conversion of ethyl acetate. Conversely, ethyl acetate significantly inhibits the oxidation of benzene but promotes the conversion of toluene. Therefore, numerical simulations of multi-component catalytic combustion reactions still require further investigation and exploration. For a long time, scholars have focused on the combustion temperature and pressure drop of the regenerator. However, research on the internal gas flow of the RCO remains relatively limited, with its turbulent effects often being neglected [21,22]. Given that gas flow significantly impacts combustion characteristics and equipment stability, further investigation is necessary.

To accurately investigate the reactions and flow within a RCO, this study proposes a multi-component catalytic combustion model coupled with a turbulence model. Numerical simulations of the flow, heat transfer, and chemical reactions inside the combustion chamber were conducted using this model. The effects of inlet gas load and equivalence ratio on the conversion rate of VOCs and temperature distribution are analyzed. Additionally, the impact mechanisms of multi-component catalytic combustion are explored.

2. Model Description

2.1. Turbulence model

The Navier-Stokes equations are fundamental for describing fluid motion. However, solving the Navier-Stokes equations directly is often impractical in industrial applications due to the complexity of fluid flows and limitations in computational resources. The Reynolds-averaged Navier-Stokes (RANS) approach addresses these challenges by decomposing flow variables into mean and fluctuating components. Combined with various turbulence models, the RANS method can efficiently simulate turbulent phenomena in engineering applications [23].

The RNG model provides an analytical formula that accounts for the viscous effects in low Reynolds number flows. This enables the RNG k-ε model to offer improved simulation results in low Reynolds number flows. Additionally, by considering turbulent vortices, the model enhances the accuracy in this aspect. As a result, it allows for a clearer understanding of the combustion phenomena and fluid flow within the oxidation furnace [24]. The equations for turbulent kinetic energy k and its dissipation rate ε are as follows:

$$\frac{\partial}{\partial t}(\rho k)+\frac{\partial}{\partial x_i}(\rho k u_i)=\frac{\partial}{\partial x_j}\left(a_k u_{\text{eff}}\frac{\partial k}{\partial x_j}\right)+G_k+G_{\text{b}}-\rho\varepsilon-Y_{\text{M}}+S_k \tag{1}$$

$$\frac{\partial}{\partial t}(\rho\varepsilon)+\frac{\partial}{\partial x_i}(\rho\varepsilon u_i)=\frac{\partial}{\partial x_j}\left(a_\varepsilon u_{\text{eff}}\frac{\partial \varepsilon}{\partial x_j}\right)+E_{1\varepsilon}\frac{\varepsilon}{k}(G_k+E_{3\varepsilon}G_{\text{b}}) - E_{2\varepsilon}\rho\frac{\varepsilon^2}{k}-R_\varepsilon+S_\varepsilon \tag{2}$$

where ρ is the fluid density; u_i is the fluid velocity vector; G_k is the turbulent kinetic energy generated by the velocity gradient; G_{b} is the turbulent kinetic energy generated by the buoyancy force; Y_{M} is the turbulent kinetic energy generated by the fluctuating expansion, the empirical constants $E_{1\varepsilon}$, $E_{2\varepsilon}$, and $E_{3\varepsilon}$ are assigned values of 1.42, 1.68, and 0.09, respectively.

2.2. Species transport model

The composition of VOCs is complex. The species transport model calculates the mass fraction of each VOC component by solving the convective diffusion equation.

$$\frac{\partial}{\partial t}(\rho Y_i)+\nabla\cdot(\rho\boldsymbol{v}_i Y_i)=-\nabla\boldsymbol{J}_i+R_i+S_{Y_i} \tag{3}$$

where, $\boldsymbol{v}_i$ represents the velocity of the diffusing species, Y_i denotes the mass fraction of species i, $\boldsymbol{J}_i$ is diffusion flux of specie i, R_i is the net formation rate of species i through chemical reactions, S_{Y_i} is the source term associated with the chemical reaction of species i.

In multicomponent systems, the Maxwell-Stefan equation can more accurately describe the diffusion behavior of each component in the mixture by calculating the diffusion mass flux [25].

$$\boldsymbol{J}_i=\sum_{j=1}^{N-1}\rho\boldsymbol{D}_{ij}\nabla Y_j+\boldsymbol{D}_{T,i}\frac{\nabla T}{T} \tag{4}$$

where $\boldsymbol{D}_{ij}$ is the binary mass diffusion coefficient of species i in species j, $\boldsymbol{D}_{T,i}$ represents the thermal diffusion coefficient for species i. The mass diffusion coefficient and thermal diffusion coefficient were calculated using kinetic theory, with the detailed calculation process presented in Ref. [26].

2.3. Porous media model

The regenerator and catalyst-packed bed contain many fine pores with complex geometries, making meshing difficult. Therefore, a porous medium model is selected to simulate the flow, heat transfer, and surface reactions within the regenerative ceramic material. Qi *et al.* [27] used a porous media model combined with a single-step methane reaction mechanism to simulate a reactor packed with ceramic monoliths, and the computational results showed good agreement with experimental data. In the Fluent porous media model, the influence of porous media on fluid flow is simulated by adding a momentum source term to the momentum equation. This source term consists of two parts: the viscous loss term and the inertial loss term.

$$S_i=-\left(\sum_{j=1}^{3}\boldsymbol{D}_{ij}\mu v_j+\sum_{j=1}^{3}\boldsymbol{C}_{ij}\rho|v|v_j\right) \tag{5}$$

where S_i is the momentum source term in the i-direction; μ is the dynamic viscosity (Pa·s); v is the gas velocity within the porous medium ($\text{m}\cdot\text{s}^{-1}$); $\boldsymbol{D}_{ij}$ and $\boldsymbol{C}_{ij}$ are specified matrices. The effective thermal conductivity is expressed as follows:

$$k_{\text{eff}}=\gamma k_{\text{f}}+(1-\gamma)k_{\text{s}} \tag{6}$$

where, k_f and k_s are the thermal conductivities of the fluid and solid, respectively. The specific heat, density, and thermal conductivity of the solid and gas phases are shown in Tables 1 and 2, respectively.

2.4. Catalytic reaction model

For reactions occurring within porous media, the source term resulting from the reaction is obtained by multiplying the reaction rate with the porosity.

$$R_i = M_{w,i} \sum_{N_R}^{r=1} \gamma \widehat{R}_{i,r} \tag{7}$$

where $M_{w,i}$ is the molecular weight of species i; γ is the porosity; $\widehat{R}_{i,r}$ is the molar formation or consumption rate of species i in reaction r. The reaction rate is expressed using the Arrhenius equation.

$$K = A_r T e^{-E/RT} \tag{8}$$

where A_r is the pre-exponential factor; E is the activation energy of the reaction ($J \cdot kmol^{-1}$); R is the universal gas constant ($J \cdot kmol^{-1} \cdot K^{-1}$).

The complexity of the model and the substantial computational demands associated with multistep reactions often lead to convergence difficulties during numerical simulations. While the single-step reaction mechanism neglects intermediate elementary reactions, the resulting computational errors are generally within acceptable limits. When the focus is on combustion efficiency and final products rather than detailed reaction processes and intermediate species, the single-step reaction mechanism is deemed sufficient.

The catalytic properties of precious metals are the preferred choice for the decomposition of VOCs. Generally, noble metal catalysts have higher low-temperature activity than non-noble metal catalysts in the catalytic oxidation of VOCs [4,28–30]. Palladium, in particular, shows higher activity in its oxide form [31]. Therefore, palladium oxide was selected as the catalyst in this study. The chemical reaction mechanism is shown in Table 3.

3. Boundary Condition and Mesh

3.1. Computational objects

The geometric model and mesh of the dual-bed regenerative catalytic oxidizer is shown in Fig. 1 and is based on the experimental setup described by Huang *et al.* [33]. The model includes rectifier sections (A1 and A2), regenerative sections (B1 and B2), and catalytic sections (C1 and C2). VOCs absorb and release energy in the regenerative sections (B1 and B2), and the combustible components undergo catalytic reactions in the catalytic sections (C1 and C2). The valve switching time is set to 2 min.

Table 1
Specific heat of solid and gas phases.

Materials	Specific heat/$J \cdot kg^{-1} \cdot K^{-1}$
CH_4	$403.58 + 9.057T - 0.0144T^2 + 1.58 \times 10^{-5}T^3 - 6.343 \times 10^{-9}T^4$
C_2H_6	$404.39 + 4.284T + 0.0016T^2 - 3.478 \times 10^{-6}T^3 + 1.268 \times 10^{-9}T^4$
C_3H_8	$169.11 + 5.032T + 0.001024T^2 - 4.008 \times 10^{-6}T^3 + 1.7428 \times 10^{-9}T^4$
O_2	$834.83 + 0.293T - 0.00015T^2 + 3.414 \times 10^{-7}T^3 - 2.278 \times 10^{-10}T^4$
CO_2	$429.93 + 1.874T - 0.002T^2 + 1.297 \times 10^{-6}T^3 - 4 \times 10^{-10}T^4$
H_2O	$1563.077 + 1.604T - 0.00293T^2 + 3.216 \times 10^{-6}T^3 - 1.157 \times 10^{-10}T^4$
N_2	$979.043 + 0.418T - 0.00118T^2 + 1.6744 \times 10^{-6}T^3 - 7.256 \times 10^{-10}T^4$
Honeycomb ceramics	$907.61 + 0.23T$

Table 2
Density and thermal conductivity of solid and gas phases.

Materials	Density/$kg \cdot m^{-3}$	Thermal conductivity/$W \cdot m^{-1} \cdot K^{-1}$
CH_4	0.6679	0.0332
C_2H_6	1.2630	0.0207
C_3H_8	1.9100	0.0177
O_2	1.2999	0.0246
CO_2	1.7878	0.0145
H_2O	0.5542	0.0261
N_2	1.1380	0.0242
Honeycomb ceramics	2500	1.9

Table 3
Reaction mechanisms [32].

Reaction	A_r	$E/J \cdot kmol^{-1}$
$CH_4 + 2O_2 \rightarrow CO_2 + 2H_2O$	29000	6.23×10^7
$C_2H_6 + 3.5O_2 \rightarrow 2CO_2 + 3H_2O$	23000	5.76×10^7
$C_3H_8 + 5O_2 \rightarrow 3CO_2 + 4H_2O$	8000	4.82×10^7

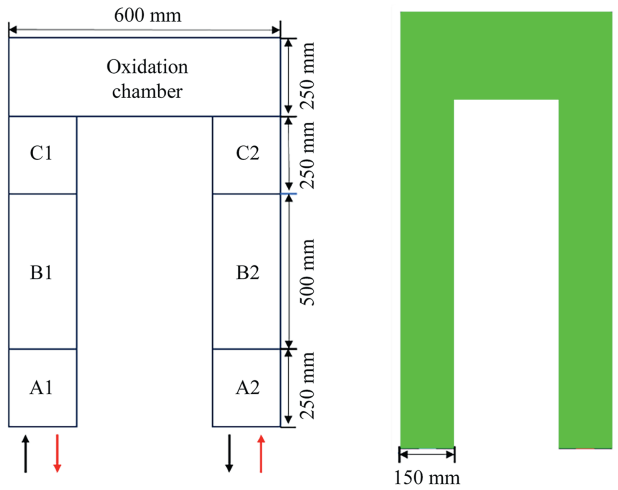

Fig. 1. RCO geometric model and mesh.

3.2. Boundary conditions and numerical methods

Typical air pollutants are light hydrocarbons, which are widely sourced from the petroleum industry and automobile exhaust [34]. The composition of the gas mixture is based on the VOCs from the Xinjiang Xintian coal gas plant, and the concentration of each component is listed in Table 4. The inlet gas temperature is set at 300 K. To minimize computational time, a linear distribution of the preheating temperature is implemented using a user-defined function (UDF).

The implicit pressure-based solver is employed, coupling pressure and velocity through the SIMPLE algorithm. The transient terms are discretized using a second-order implicit scheme, while the momentum and energy terms are discretized using a second-order upwind scheme.

3.3. Grid independence verification

Structured grids offer several advantages, including fast and high-quality mesh generation, as well as the ability to easily fit complex boundaries. These characteristics make structured grids particularly suitable for CFD simulations. Therefore, structured grids are employed in this study.

Table 4
VOCs composition.

Species	Mole fraction/%
CH_4	0.33
C_2H_6	0.21
C_3H_8	0.08
O_2	8.28

To eliminate the influence of grid numbers on the calculation results, a grid independence test is conducted. The grid numbers considered in this work include 10000, 256120, and 1081680.

The conversion rate of methane gas with a concentration of 0.003 and an equivalence ratio of 1 is used as the evaluation criterion. Fig. 2 shows the conversion rate distribution of methane along the axis of the oxidation furnace for different mesh resolutions. Considering both accuracy and computational cost, a mesh with 256120 cells is selected.

3.4. Model verified by the benchmark

The results are compared with the experimental results [35] under the same operating conditions. In both experiments and simulations, the inlet gas is toluene with a concentration of 200 $cm^3 \cdot m^{-3}$, and the valve switching time is set to 120 s. The results indicate that the outlet temperature and conversion rate closely

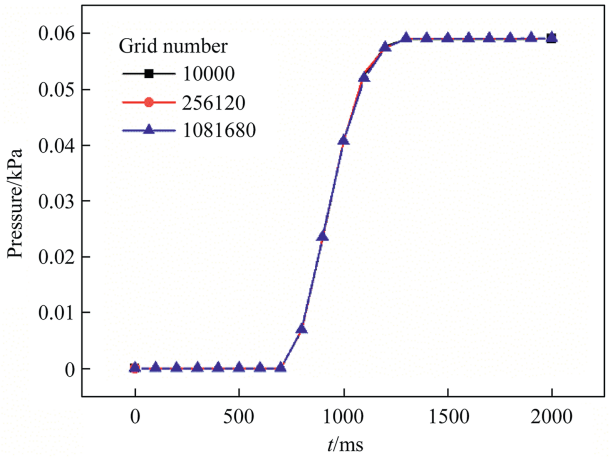

Fig. 2. Grid independence validation.

Table 5
Comparison results between simulated and experimental values.

	T_{set}/K	v_{in}/m·s^{-1}	T_{in}/K	T_{out}/K	ω/% (mass)
Experiment	573	0.37	302.0	319.8	92.2
Simulation				318.8	91.4
Experiment	573	0.74	301.0	322.7	90.2
Simulation				324.2	89.8
Experiment	673	0.37	304.0	325.0	92.8
Simulation				324.9	93.5
Experiment	673	0.74	303.0	331.5	90.4
Simulation				332.2	87.9

T_{set}: Setting temperature of oxidizing furnace. T_{in}: Inlet gas temperature. T_{out}: Outlet gas temperature. ω: Reactant conversion rate.

match the experimental data, thereby demonstrating satisfactory validation. The comparison results are shown in Table 5.

4. Results and Discussion

4.1. Effect of intake load

The inlet load, a core parameter in the design of combustion furnaces, directly influences the efficiency of pollutant treatment. In this study, dynamic control of the load is achieved by adjusting the inlet gas velocity. Under constant inlet VOC composition, concentration, and temperature, simulations were performed at varying inlet gas velocities to investigate their impact on VOC conversion efficiency and distribution characteristics within the RCO. The inlet conditions were specified as follows: an equivalence ratio of 0.21, an exhaust gas temperature of 300 K, and an inlet velocity ranging from 0.1 to 1.7 m·s^{-1}.

Fig. 3 shows the distribution of gas velocity and turbulent kinetic energy along the centerline of the RCO bed layer, excluding the oxidation chamber cavity, at inlet gas velocities ranging from 0.1 to 1.7 m·s^{-1}. Upon entering the B1 section, the exhaust gas encounters significant resistance from the porous medium framework, resulting in a substantial reduction in velocity. With increasing inlet gas velocity, the obstructive effect becomes more pronounced. At an inlet gas velocity of 1.7 m·s^{-1}, the gas velocity drops significantly to approximately 0.5 m·s^{-1}. In contrast, at an inlet velocity of 0.1 m·s^{-1}, the change in gas velocity is relatively small. Subsequently, the velocity gradually recovers to a level close to the inlet velocity due to fluid inertia. According to Darcy's law, the velocity is directly proportional to the pressure gradient. As the flow approaches the outlet, the pressure gradient decreases,

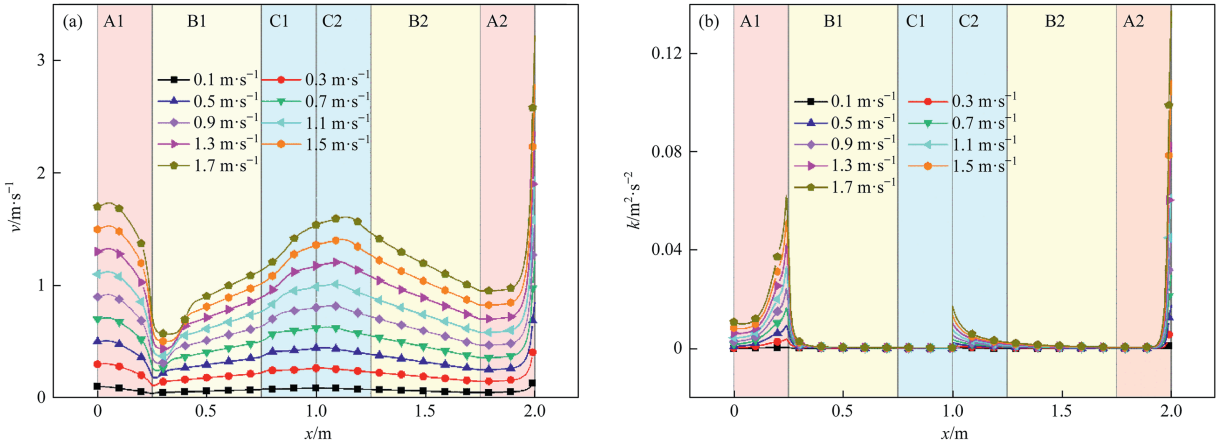

Fig. 3. (a) Gas velocity and (b) turbulent kinetic energy along the centerline of the RCO bed layer (excluding the oxidation chamber) at inlet gas velocities ranging from 0.1 to 1.7 m·s^{-1}.

reducing the velocity. At the outlet, the abrupt increase in cross-sectional area causes the gas velocity to accelerate, similar to fluid flowing through a nozzle.

The variation in turbulent kinetic energy is mainly concentrated in the inlet and outlet regions, as shown in Fig. 3(b). At the inlets of sections B1 and C2, abrupt changes in the magnitude and direction of gas velocity lead to a marked increase in turbulent kinetic energy. As the inlet gas velocity increases, the collision frequency between gas molecules and wall surfaces rises. The turbulent kinetic energy at the inlet of B1 increases from 4×10^{-4} $m^2 \cdot s^{-2}$ to approximately 0.06 $m^2 \cdot s^{-2}$, while at the inlet of C2, it rises from 3.6×10^{-4} $m^2 \cdot s^{-2}$ to 0.017 $m^2 \cdot s^{-2}$. Upon entering the porous medium, the frictional resistance between the pore walls and the gas continuously dissipates kinetic energy, causing a gradual decrease in turbulent kinetic energy.

Fig. 4(a) shows the VOCs conversion rates and experimental comparisons under different inlet flow velocities, while Fig. 4(b) presents the maximum reaction rates of individual VOCs

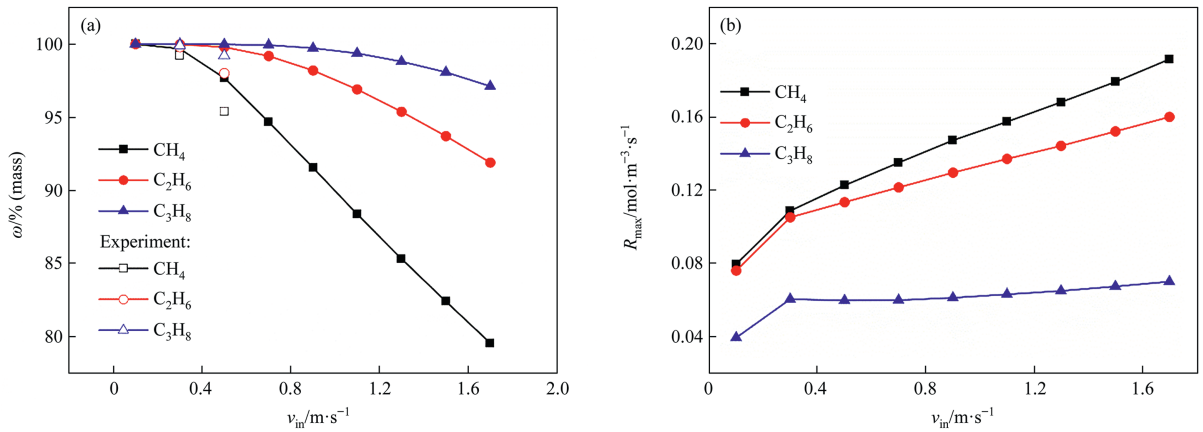

Fig. 4. (a) The conversion rates of VOCs components and their experimental comparisons, (b) as well as the maximum reaction rates, under different inlet flow rates are presented.

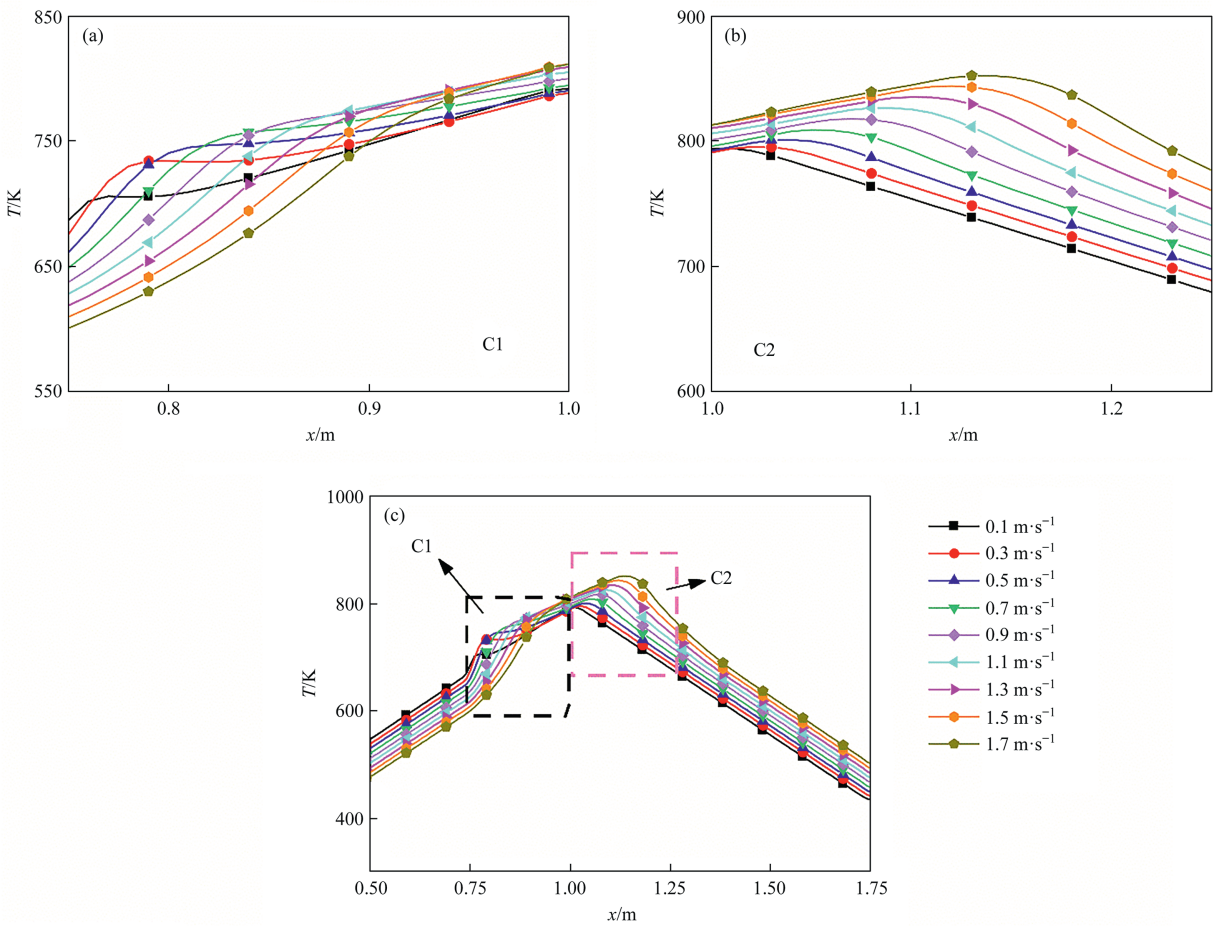

Fig. 5. Temperature distribution under different inlet gas velocities: (a) C1 catalytic section; (b) C2 catalytic section; (c) Entire porous medium region.

components under different inlet flow rates. As the inlet gas velocity increases, the mass transfer rate of the gas to the catalyst surface is enhanced. The number of reactant molecules per unit volume also increases, leading to higher reaction rates for all three components. However, the conversion rate of VOCs decreases, indicating that it is primarily governed by the residence time. Methane molecules, being relatively small, are more likely to reach the catalyst surface. Consequently, methane exhibits the largest increase in reaction rate, rising from 0.08 $mol \cdot m^{-3} \cdot s^{-1}$ to approximately 0.2 $mol \cdot m^{-3} \cdot s^{-1}$. Ethane exhibits the second-highest reaction rate enhancement, followed by propane which shows the smallest increase at approximately 0.02 $mol \cdot m^{-3} \cdot s^{-1}$. When the inlet gas velocity increases from 0.1 $m \cdot s^{-1}$ to 1.7 $m \cdot s^{-1}$, the conversion rate of methane decreases by 22%, ethane by 8%, and propane by less than 5%. This indicates that the conversion rate of methane is more sensitive to changes in flow velocity. The C—H bonds in methane are relatively stable and have a higher activation energy, requiring a longer residence time for complete reaction. In contrast, ethane and propane have relatively higher reaction activities and are less affected by flow velocity.

Fig. 5 shows the radial temperature distribution within the reactor bed. As the inlet gas velocity increases, the high-temperature zone in the reaction region shifts backward. Specifically, when the gas velocity increases from 0.1 $m \cdot s^{-1}$ to 0.3 $m \cdot s^{-1}$, a significant temperature rise is observed in the reaction zone compared to other velocities, leading to an increased reaction rate. Additionally, higher inlet gas velocities result in higher outlet temperatures. The increase in the intake flow rate raises the concentration of reactants, intensifying the catalytic reaction and increasing the heat released. This results in higher outlet temperatures.

Figs. 6 and 7 illustrate the concentration distribution and reaction zone distribution of the three reactants in the catalytic section under different inlet flow rates. At low inlet flow rates, the exhaust gas can be completely reacted in catalytic zone C1. As the inlet flow rate increases, the residence time decreases, causing the reaction zone to gradually expand. Unreacted reactants then enter C2 to continue the reaction. Moreover, as the flow rate increases, the high-reactivity reaction zone gradually shifts backward. Methane requires the largest reaction space, followed by ethane. This trend is closely related to the reaction kinetics of each substance. When the inlet flow rate is between 0.1 and 1.7 $m \cdot s^{-1}$, propane can be almost completely reacted, achieving a conversion rate of over 97%. Although the initial concentration of ethane is higher than that of methane, its higher conversion rate means that at an inlet flow rate of 1.7 $m \cdot s^{-1}$, the mass fraction of unreacted ethane is only half that of methane.

4.2. Influence of equivalence ratios

The fuel-to-oxygen equivalence ratio is a key factor influencing combustion efficiency and stability. It must be optimized based on the specific combustion system and application requirements. In this study, simulations were conducted under the conditions of an inlet temperature of 300 K and an inlet velocity of 0.1 $m \cdot s^{-1}$, for equivalence ratios ranging from 0.2 to 2.0. During this process, the molar fractions of methane, ethane, and propane were kept constant, and the equivalence ratio was adjusted by varying the

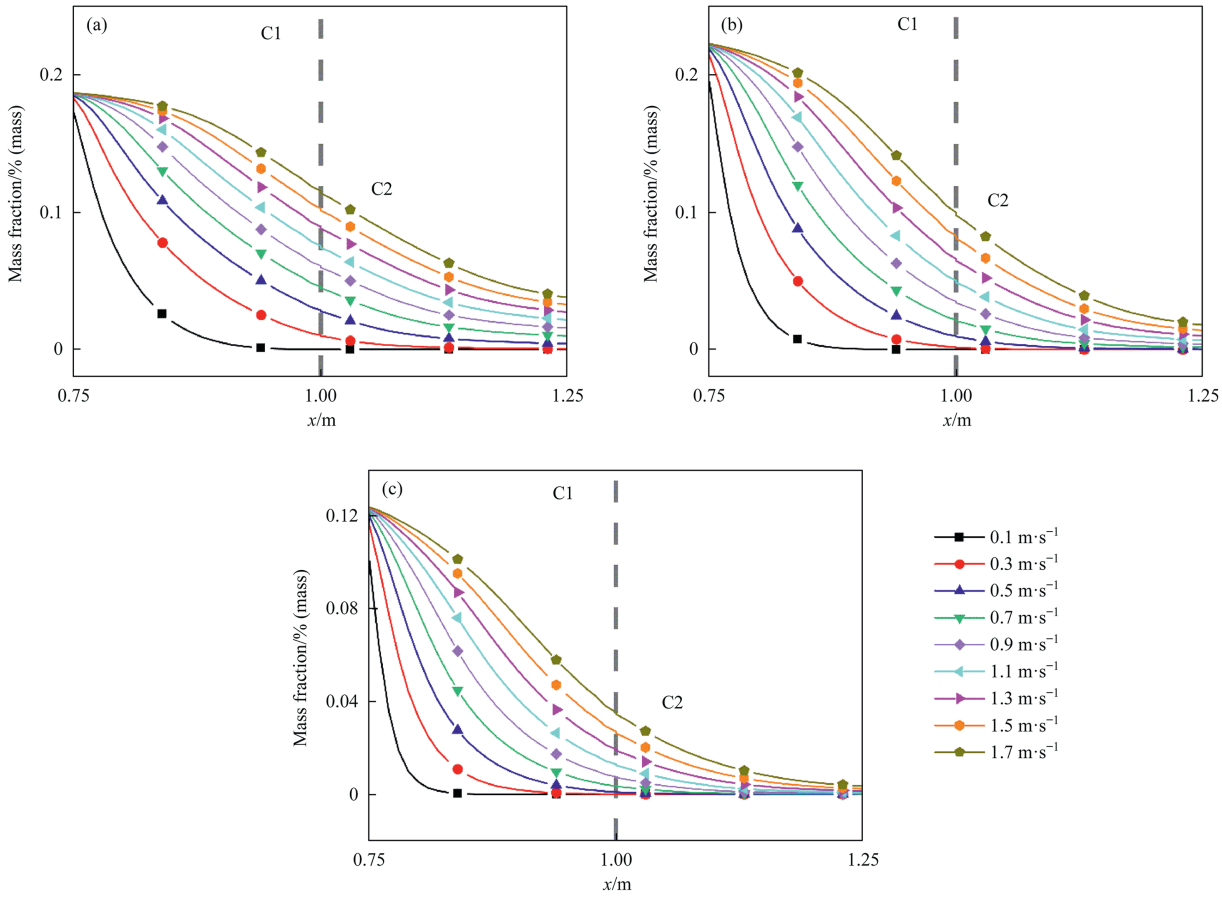

Fig. 6. Concentration distribution at different inlet flow rates: (a) methane; (b) ethane; (c) propane.

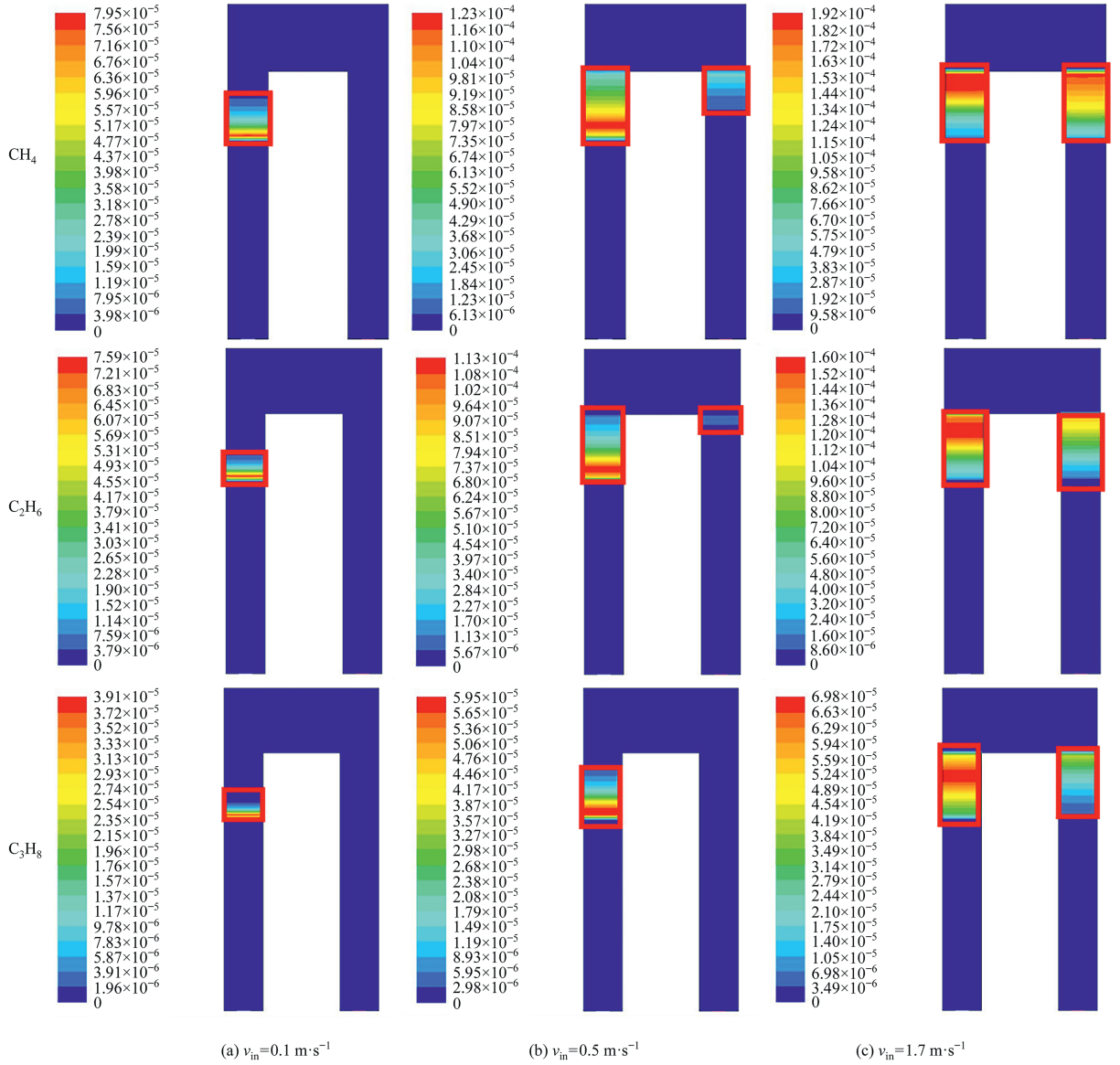

Fig. 7. Contour map of VOCs surface reaction rate (kmol·m^{-3}·s^{-1}).

oxygen content. These simulations investigated the impact of the equivalence ratio on VOC conversion efficiency and distribution characteristics within the RCO. The equivalence ratio is defined as follows:

$$\phi = \frac{(C_xH_y : Air)_{real}}{(C_xH_y : Air)_{stoich}} \tag{9}$$

where $(C_xH_y : Air)_{real}$ is the mass ratio of fuel to air actually supplied, $(C_xH_y : Air)_{stoich}$ is the stoichiometric or theoretical fuel-air ratio. When $\phi = 1$, the fuel and air are in perfect stoichiometric proportion for complete combustion. Values of $\phi > 1$ indicate excess fuel and insufficient air (rich combustion), while $\phi < 1$ represents excess air and insufficient fuel (lean combustion).

Fig. 8(a) and (b) show the conversion rate of VOCs and its variation rate under different equivalence ratios. The results indicate that increasing the equivalence ratio significantly inhibits the catalytic conversion of the three gases. At an equivalence ratio of 2.0, the conversion efficiency of methane decreases to below 40%, while the conversion rates of ethane and propane are approximately 50% and 70%, respectively. This suggests a positive correlation between the length of the alkane carbon chain and the stability of conversion. Further analysis revealed that the conversion rates of the various components exhibit a nonlinear decay trend with increasing equivalence ratio. The rate of decline is initially steep and then gradually flattens. The conversion rate of methane decreases most significantly at an equivalence ratio of 1.0, with a reduction of over 60%. The conversion rate of ethane drops most rapidly at an equivalence ratio of 1.2, with a decrease of approximately 40%. The highest rate of decline in the conversion rate of propane occurs at an equivalence ratio of 1.4. As shown in Fig. 8(c), the oxygen conversion rate remains above 90% once the equivalence ratio ϕ exceeds 1.0, indicating that oxygen molecules are nearly completely consumed under fuel-rich conditions. These data suggest that low-carbon alkanes are more sensitive to oxygen-deficient environments.

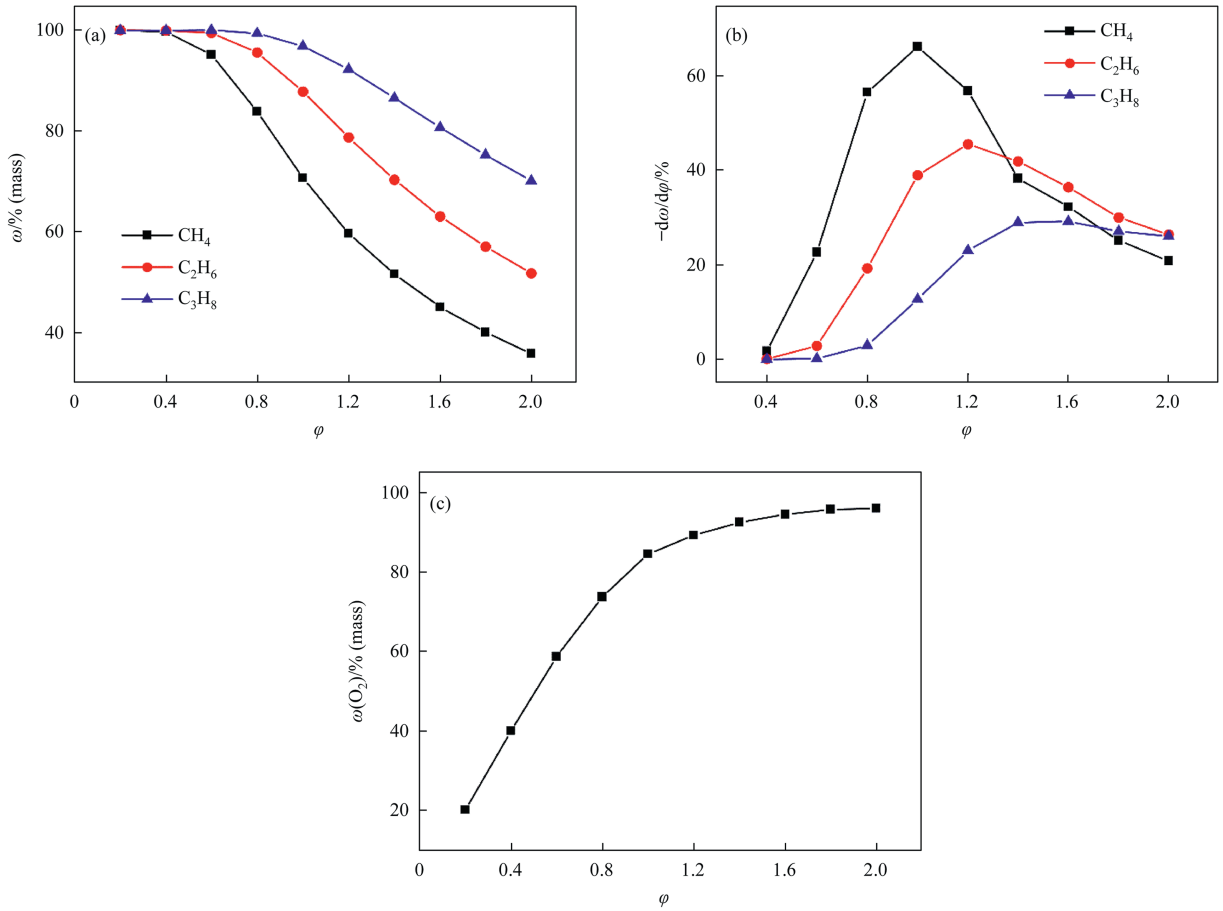

Fig. 8. Reaction characteristics of VOCs at different equivalence ratios: (a) conversion rates of three alkanes, (b) variation rates of conversion rates of three alkanes, (c) oxygen conversion rate.

4.3. Comparison of combustion characteristics of mixed VOCs and single component gases

To more clearly illustrate the necessity of using mixed hydrocarbons in the simulated regenerative catalytic oxidation furnace for VOCs treatment, the multi-component VOCs were converted into single-component methane, ethane, and propane based on the same heat value while maintaining the same equivalence ratio. A comparative analysis was then conducted. The inlet temperature for the simulation conditions is 300 K, with an inlet velocity ranging from 0.1 to 1.7 $m \cdot s^{-1}$. The gas compositions for the four operating conditions are shown in Table 6.

The conversion and reaction rates of these compounds were compared, and the results are shown in Fig. 9. Comparisons of catalytic combustion characteristics between mixed gases and single-component gases reveal consistent trends in conversion and reaction rates across the reactions. As the inlet gas velocity increases, conversion rates decrease while reaction rates increase. Additionally, the conversion rate of methane in mixed gases is significantly higher than that in single-component gas, whereas the conversion rates of ethane and propane in mixed gases are slightly lower than those in single-component gas. As the inlet flow rate increases, the difference in methane conversion rates between the mixed gas and single-component methane grows. At an inlet flow rate of 1.8 $m \cdot s^{-1}$, the methane conversion rate in the mixed VOCs is approximately 40% higher than that of single-component methane. These findings indicate that mixed gases promote the reaction of methane but inhibit the reactions of ethane and propane.

Table 6
The composition of VOCs under four operating conditions at constant heat value.

Species	Operating condition 1	Operating condition 2	Operating condition 3	Operating condition 4
CH_4/%	0.33	0.915		
C_2H_6/%	0.21		0.51	
C_3H_8/%	0.08			0.352
O_2/%	8.28	9.15	8.92	8.8

Fig. 10 shows the temperature distribution in the catalytic reaction zone for mixed exhaust gases and single-component exhaust gases under different inlet flow rates. Although the high-temperature zones resulting from combustion heat release differ under different gas flow rates, the reaction temperatures of ethane and propane are always higher than that of methane. Among them, propane combustion releases the most heat, approximately 80 K higher than that of methane. The combustion temperature of mixed gases in the reaction zone is significantly higher than that of methane combustion alone but lower than the combustion temperatures of ethane and propane as single components. This suggests that the addition of ethane and propane to methane significantly enhances the combustion temperature, thereby promoting chemical reactions and effectively improving methane conversion efficiency.

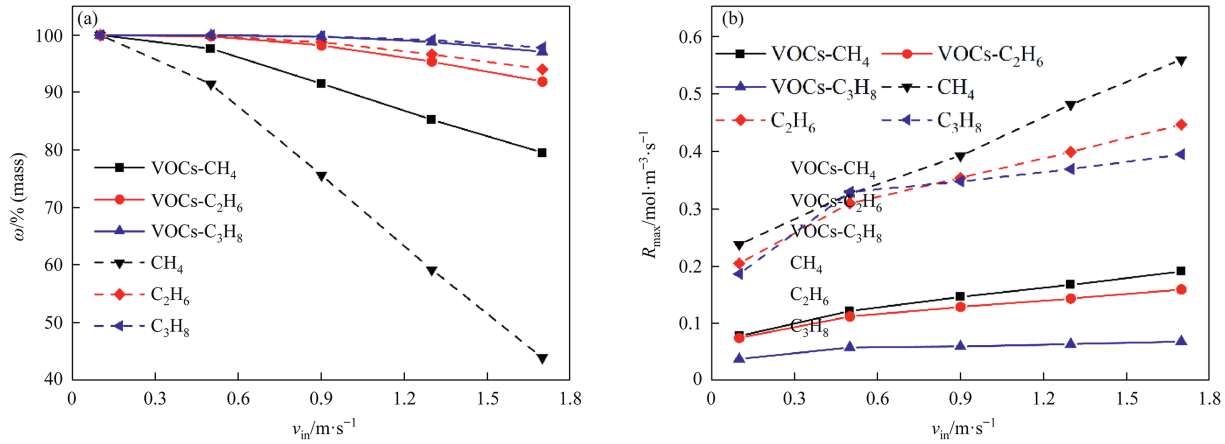

Fig. 9. Comparison of (a) conversion rates and (b) reaction rates of mixed alkanes and single-component alkanes in VOCs under different inlet flow rates, with single-component alkanes calculated based on the calorific values and volume fractions of the mixed alkanes.

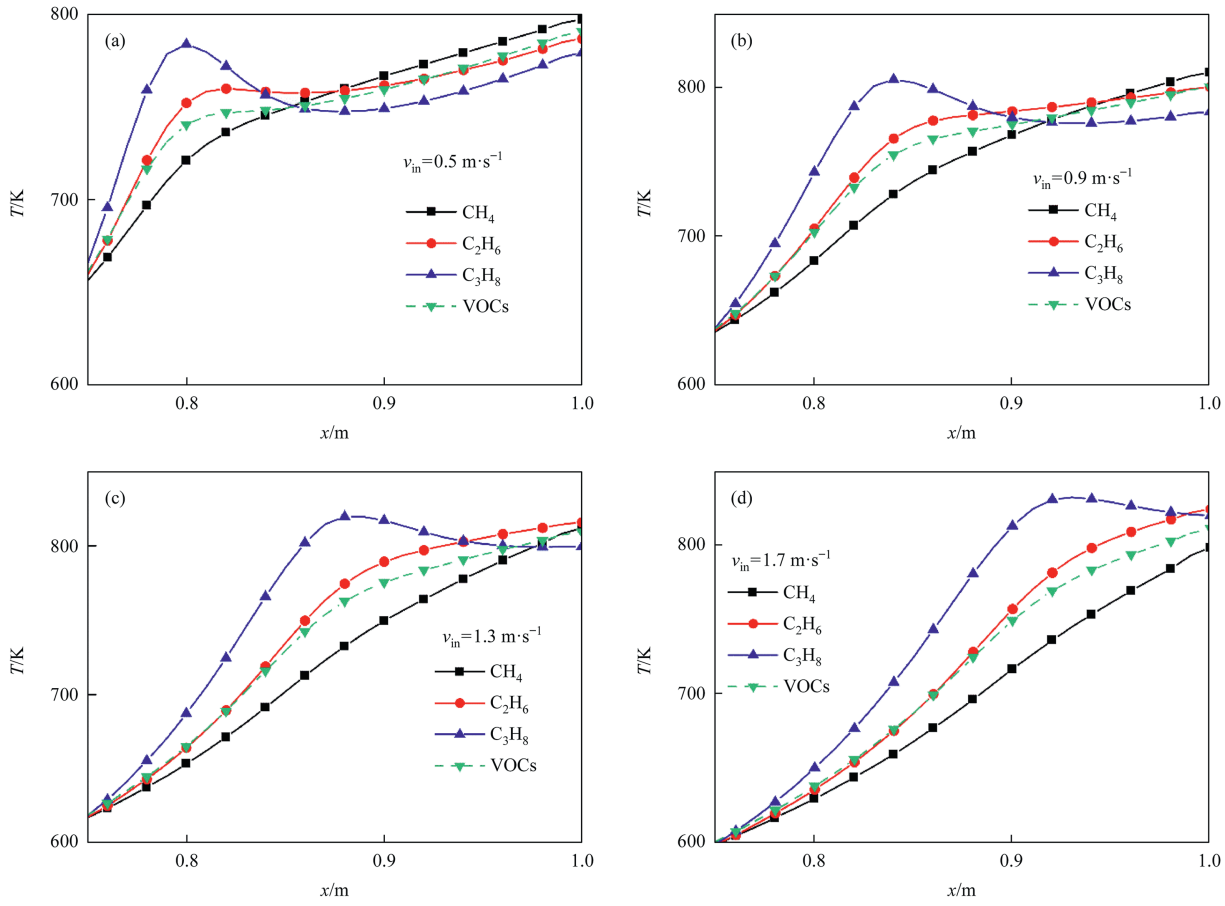

Fig. 10. Temperature distribution of mixed exhaust gas and single-component exhaust gas at different inlet flow rates: (a) $v_{in} = 0.5\ m \cdot s^{-1}$, (b) $v_{in} = 0.9\ m \cdot s^{-1}$, (c) $v_{in} = 1.3\ m \cdot s^{-1}$, (d) $v_{in} = 1.7\ m \cdot s^{-1}$.

4.4. Dual optimization of preheating temperature and intake air temperature

In the above study, it was found that among the mixed VOC gases of methane, ethane, and propane, methane conversion is most challenging when the gas velocity and equivalence ratio are increased. Specifically, the conversion rate of methane decreases most rapidly under these conditions. To enhance methane conversion, the experimental conditions are optimized by maintaining a constant inlet VOC composition and increasing both the preheating and inlet temperatures at an inlet flow rate of 0.7 $m \cdot s^{-1}$.

Fig. 11 shows the methane conversion rates achieved by varying the preheating temperature and inlet temperature. Both preheating and inlet temperatures exhibit a positive correlation with methane conversion rates. Within the preheating temperature

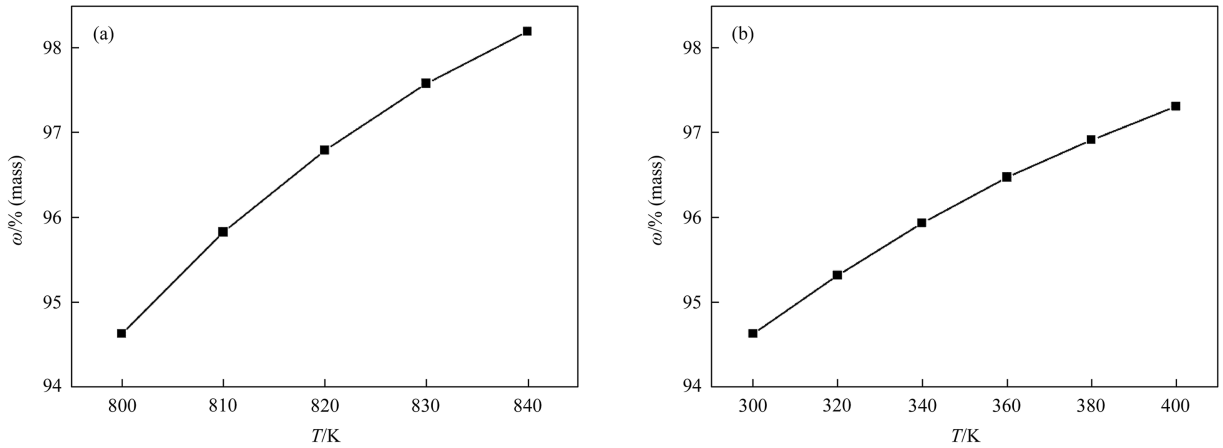

Fig. 11. Conversion of CH_4 at different (a) preheating temperatures and (b) at different inlet temperatures.

rise, the methane conversion rate increases from approximately 94.5% to around 98%. This indicates that within this temperature range of 800 K to 840 K, increasing the preheating temperature enhances the reaction rate and effectively improves methane oxidation efficiency. As the inlet temperature increases, the methane conversion rate rises from 94.5% to approximately 97%. This increase is less pronounced compared to that achieved by raising the preheating temperature. When the gas enters the preheated reactor, its higher initial temperature reduces the energy input required to reach the reaction temperature, allowing the gas to achieve the desired temperature more quickly. In comparison, increasing the preheating temperature can achieve a higher conversion rate improvement with lower energy consumption.

Fig. 12 shows the radial temperature distribution inside the oxidation furnace under different preheating temperatures and inlet gas temperatures. The preheating temperature increase raises the axial temperature to some extent, with the first peak indicating the heat released during combustion. This suggests that higher preheating temperatures lead to greater heat release during the reaction. Increasing the intake air temperature has little impact on the overall temperature distribution. However, gases with higher intake air temperatures react slightly faster, resulting in a more forward heat release position.

As revealed in Sections 4.1 and 4.2, methane requires a longer residence time or a larger reaction zone for conversion compared to ethane and propane. Therefore, this section investigates the impact of the catalytic section length L on the methane conversion rate by adjusting it. The simulation conditions are an inlet velocity of 0.7 $m \cdot s^{-1}$, an inlet temperature of 300 K, and an equivalence ratio of 0.2. Fig. 13 shows the methane conversion rates under different catalytic section lengths. As the catalytic section length increases gradually from 250 mm to 350 mm, the methane conversion rate exhibits a stable upward trend, rising from 94% to 99%. This change indicates that increasing the length of the catalytic

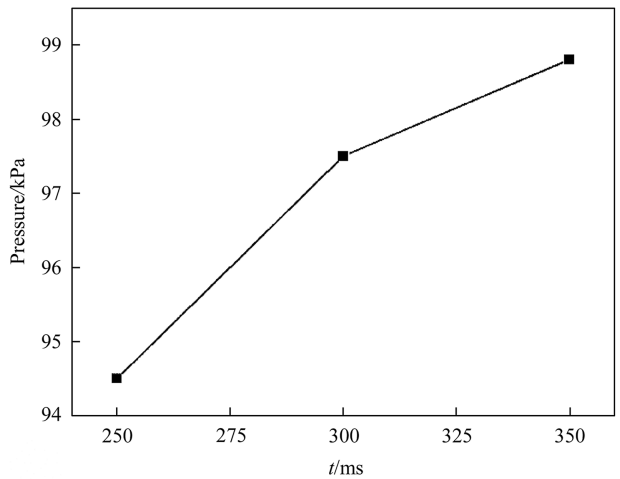

Fig. 13. Conversion rate of methane at different catalytic section lengths.

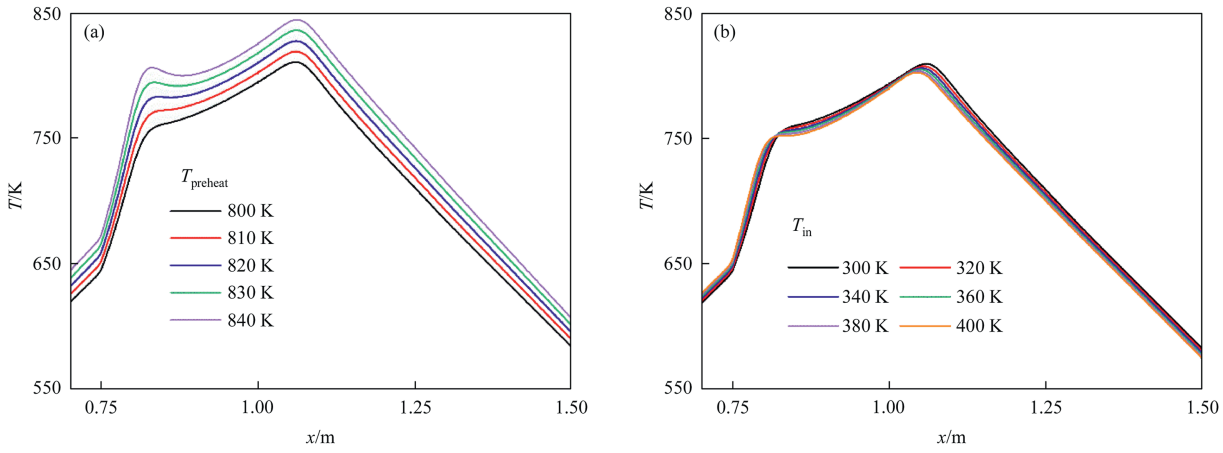

Fig. 12. Radial temperature distribution of oxidizer (a) at different preheating temperatures and (b) at different inlet temperatures.

section can significantly enhance the conversion efficiency of methane. This improvement is primarily attributed to two factors: First, the extended catalytic section length directly increases the residence time of the gas within the catalytic reaction zone, facilitating more complete contact between methane molecules and the catalyst's active sites. Second, a longer catalytic section offers a larger distribution of active sites, which enhances the diffusion and mass transfer processes of the reactants and thereby promotes the deep oxidation of methane. Moreover, as the catalytic section length increases from 300 mm to 350 mm, the growth trend of the conversion rate gradually levels off. This suggests that there may be an optimal range for the catalytic section length. Beyond this range, further increases in length have limited effects on enhancing the conversion rate and may instead lead to increased system pressure drop and energy consumption.

5. Conclusions

This paper presents a multi-component catalytic combustion model coupled with a turbulence model. This model is used to investigate the flow, heat transfer, and catalytic reaction characteristics of the catalytic transformation process of multi-component hydrocarbon-containing VOCs in a regenerative catalytic oxidizer. The study reveals the influence mechanisms of inlet flow velocity and equivalence ratio on the conversion rates of each VOC component and the combustion temperature. It also explores the interactions between the components during the catalytic reaction process.

The results indicate that in the mixed VOCs, methane is the most sensitive to changes in operating conditions, while ethane and propane are relatively stable. At an inlet gas flow rate of 1.7 $m \cdot s^{-1}$, the conversion rates of ethane and propane can both be maintained above 90%, while the conversion rate of methane is only around 78%. This difference is primarily due to the high stability of the C—H bonds in methane molecules, which leads to a higher activation energy and necessitates a longer residence time for complete reaction. Moreover, the oxygen concentration significantly impacts the conversion rate of methane. As the equivalence ratio increases, the conversion rate of methane drops most rapidly, followed by that of ethane. Further investigation into the interaction mechanisms among multi-component hydrocarbons revealed that adding ethane and propane significantly enhances methane conversion by increasing the reaction temperature, while slightly inhibiting the conversion rates of ethane and propane themselves. To increase the conversion rate of the difficult-to-convert component methane, the preheating temperature, the inlet gas temperature, and the height of the catalyst bed were adjusted, respectively. Among these adjustments, increasing the preheating temperature and the height of the catalyst bed had a more significant effect on improving the conversion rate of methane.

CRediT Authorship Contribution Statement

Yujie Kang: Writing – original draft, Validation, Investigation. Guangrun Yang: Writing – review & editing. Jingxiao Wang: Writing – review & editing. Zhongjie Shen: Writing – review & editing. Jianliang Xu: Writing – review & editing, Resources, Funding acquisition, Conceptualization. Zhenghua Dai: Project administration, Funding acquisition. Haifeng Liu: Supervision, Project administration, Funding acquisition.

Data Availability

Data will be made available on request.

Declaration of Competing Interest

The authors declare that they have no known competing financial interests or personal relationships that could have appeared to influence the work reported in this paper.

Acknowledgements

This research was financially supported by National Key Research & Development Program of China (2022YFB4101500).

Nomenclature

A_r	pre-exponential factor
$\boldsymbol{D}_{ij}$	binary mass diffusion coefficient of species *i* in species *j*
$\boldsymbol{D}_{T,i}$	the thermal diffusion coefficient for species *i*
E	activation energy of the reaction, $J \cdot kmol^{-1}$
G_b	turbulent kinetic energy generated by the buoyancy force
G_k	turbulent kinetic energy generated by the velocity gradient
$\boldsymbol{J}_i$	diffusion flux of specie *i*
k	turbulent kinetic energy, $m^2 \cdot s^{-2}$
k_f	thermal conductivity of the fluid
k_s	thermal conductivity of the solid
$M_{w,i}$	molecular weight of species *i*
R	universal gas constant, $J \cdot kmol^{-1} \cdot K^{-1}$
R_i	net formation rate of species *i*
$\widehat{R_{i,r}}$	molar formation or consumption rate of species *i* in reaction *r*
S_{Y_i}	source term associated with the chemical reaction of species *i*
T	temperature, K
$\boldsymbol{v}_i$	velocity, $m \cdot s^{-1}$
Y_i	mass fraction of species *i*
Y_M	turbulent kinetic energy generated by the fluctuating expansion
γ	porosity
ε	turbulent dissipation rate
μ	dynamic viscosity, $Pa \cdot s$
ρ	density, $kg \cdot m^{-3}$
ω	conversion rate
ϕ	equivalence ratio

Subscripts and Superscripts

in	at the inlet
i	the *i*-th species
out	at the outlet

References

[1] Statistical Communiqué of the National Economic and Social Development in 2024, National Bureau of Statistics of China, 2025.
[2] Y.F. Liu, L.W. Kong, X.G. Liu, Y.P. Zhang, C.L. Li, Y.Y. Zhang, C. Zhang, Y. Qu, J.L. An, D.P. Ma, Q.W. Tan, M. Feng, S.P. Zha, Characteristics, secondary transformation, and health risk assessment of ambient volatile organic compounds (VOCs) in urban Beijing, China, *Atmos. Pollut. Res.* 12 (3) (2021) 33–46.
[3] S.W. Kim, S.A. McKeen, G.J. Frost, S.H. Lee, M. Trainer, A. Richter, W.M. Angevine, E. Atlas, L. Bianco, K.F. Boersma, J. Brioude, J.P. Burrows, J. de Gouw, A. Fried, J. Gleason, A. Hilboll, J. Mellqvist, J. Peischl, D. Richter, C. Rivera, T. Ryerson, S. te Lintel Hekkert, J. Walega, C. Warneke, P. Weibring, E. Williams, Evaluations of NO_x and highly reactive VOC emission inventories in Texas and their implications for ozone plume simulations during the Texas air quality study 2006, *Atmos. Chem. Phys.* 11 (22) (2011) 11361–11386.
[4] Z.X. Zhang, Z. Jiang, W.F. Shangguan, Low-temperature catalysis for VOCs removal in technology and application: a state-of-the-art review, *Catal. Today* 264 (2016) 270–278.

[5] B. Han, R. Lang, B.T. Qiao, A.Q. Wang, T. Zhang, Highlights of the major progress in single-atom catalysis in 2015 and 2016, *Chin. J. Catal.* 38 (9) (2017) 1498–1507.
[6] H.B. Huang, Y. Xu, Q.Y. Feng, D.Y.C. Leung, Low temperature catalytic oxidation of volatile organic compounds: a review, *Catal. Sci. Technol.* 5 (5) (2015) 2649–2669.
[7] L.L. Xu, D. Chen, J.L. Qu, L.Y. Wang, J.Y. Tang, H. Liu, J. Yang, Replacement reaction-based synthesis of supported palladium catalysts with atomic dispersion for catalytic removal of benzene, *J. Mater. Chem. A* 6 (35) (2018) 17032–17039.
[8] I.E. Sungkono, H. Kameyama, T. Koya, Development of catalytic combustion technology of VOC materials by anodic oxidation catalyst, *Appl. Surf. Sci.* 121-122 (1997) 425–428.
[9] C. Moreno-Castilla, A.F. Pérez-Cadenas, Carbon-based honeycomb monoliths for environmental gas-phase applications, *Materials* 3 (2) (2010) 1203–1227.
[10] H. Mei, C.Y. Li, H. Liu, S.F. Ji, Simulation of catalytic combustion of methane in a monolith honeycomb reactor, *Chin. J. Chem. Eng.* 14 (1) (2006) 56–64.
[11] Y.H. Liu, X.J. Li, Q. Xiao, X.F. Jiang, W.L. Dong, X.Y. Chen, Y.Y. Feng, Simulation study on catalytic oxidation of low concentration mine gas in an oxidation device, *Sci. Rep.* 15 (1) (2025) 25.
[12] S. Kumaresh, K. Young, Numerical investigation of catalytic combustion in a honeycomb monolith with lean methane and air premixtures over the platinum catalyst, *Int. J. Therm. Sci.* 138 (2019) 304–313.
[13] S. Tischer, C. Correa, O. Deutschmann, Transient three-dimensional simulations of a catalytic combustion monolith using detailed models for heterogeneous and homogeneous reactions and transport phenomena, *Catal. Today* 69 (1–4) (2001) 57–62.
[14] Z.K. Sang, Z.M. Bo, X. Liu, Y. Weng, Characteristic analysis of a rotary regenerative type catalytic combustion reactor for ultra low calorific value gas, *J. Energy Resour. Tech.* 139 (6) (2017) 062208.
[15] Y.F. Yan, S. Feng, Z.Z. Huang, L. Zhang, W.L. Pan, L.X. Li, Z.Q. Yang, Thermal management and catalytic combustion stability characteristics of premixed methane/air in heat recirculation meso-combustors, *Int. J. Energy Res.* 42 (3) (2018) 999–1012.
[16] B.O. Arani, C.E. Frouzakis, J. Mantzaras, F. Lucci, K. Boulouchos, Direct numerical simulation of turbulent channel-flow catalytic combustion: effects of Reynolds number and catalytic reactivity, *Combust. Flame* 187 (2018) 52–66.
[17] S. Scirè, S. Minicò, C. Crisafulli, S. Galvagno, Catalytic combustion of volatile organic compounds over group IB metal catalysts on Fe_2O_3, *Catal. Commun.* 2 (6–7) (2001) 229–232.
[18] S. Ordóñez, L. Bello, H. Sastre, R. Rosal, F.V. Díez, Kinetics of the deep oxidation of benzene, toluene, *n*-hexane and their binary mixtures over a platinum on γ-alumina catalyst, *Appl. Catal. B Environ.* 38 (2) (2002) 139–149.
[19] Y.S. Xia, L. Xia, Y.X. Liu, T. Yang, J.G. Deng, H.X. Dai, Concurrent catalytic removal of typical volatile organic compound mixtures over Au-Pd/α-MnO_2 nanotubes, *J. Environ. Sci. (China)* 64 (2018) 276–288.
[20] C. He, P. Li, J. Cheng, Z.P. Hao, Z.P. Xu, A comprehensive study of deep catalytic oxidation of benzene, toluene, ethyl acetate, and their mixtures over Pd/ZSM-5 catalyst: mutual effects and kinetics, *Water Air Soil Pollut.* 209 (1) (2010) 365–376.
[21] K. Gosiewski, A. Pawlaczyk-Kurek, Aerodynamic CFD simulations of experimental and industrial thermal flow reversal reactors, *Chem. Eng. J.* 373 (2019) 1367–1379.
[22] M.Z. Xie, J.R. Shi, Y.B. Deng, H. Liu, L. Zhou, Y.N. Xu, Experimental and numerical investigation on performance of a porous medium burner with reciprocating flow, *Fuel* 88 (1) (2009) 206–213.
[23] N.F. Jouybari, M. Maerefat, T. Staffan Lundström, M.E. Nimvari, Z. Gholami, A general macroscopic model for turbulent flow in porous media, *J. Fluids Eng.* 140 (2018) 011201.
[24] W.-J. Liang, D. Liu, S.-D. Ren, Q.-L. Li, CFD simulation and optimization of flow-reverse catalytic-combustion reactor, *J. Environ. Eng.* 146 (6) (2020) 04020043.
[25] K. Sutton, P. Gnoffo, Multi-component Diffusion with Application to Computational aerothermodynamics. In: 7th AIAA/ASME Joint Thermophysics and Heat Transfer Conference. Albuquerque, NM, AIAA, Reston, Virginia, 1998.
[26] J.O. Hirschfelder, C.F. Curtiss, R.B. Bird, Molecular theory of gases and liquids, *Phys. Today* 8 (3) (1955) 17.
[27] X.N. Qi, Y.Q. Liu, H.Q. Xu, Z.Y. Liu, R.X. Liu, Modeling thermal oxidation of coal mine methane in a non-catalytic reverse-flow reactor, *Strojniski Vestnik* 60 (7–8) (2014) 495–505.
[28] M. Jabłońska, A. Król, E. Kukulska-Zając, K. Tarach, V. Girman, L. Chmielarz, K. Góra-Marek, Zeolites Y modified with palladium as effective catalysts for low-temperature methanol incineration, *Appl. Catal. B Environ.* 166 (167) (2015) 353–365.
[29] C.B. Zhang, H. He, K.I. Tanaka, Catalytic performance and mechanism of a Pt/TiO_2 catalyst for the oxidation of formaldehyde at room temperature, *Appl. Catal. B Environ.* 65 (1–2) (2006) 37–43.
[30] P. Gélin, M. Primet, Complete oxidation of methane at low temperature over noble metal based catalysts: a review, *Appl. Catal. B Environ.* 39 (1) (2002) 1–37.
[31] A.K. Neyestanaki, F. Klingstedt, T. Salmi, D.Y. Murzin, Deactivation of post-combustion catalysts, a review, *Fuel* 83 (4–5) (2004) 395–408.
[32] Y.X. Xin, H. Wang, C.K. Law, Kinetics of catalytic oxidation of methane, ethane and propane over palladium oxide, *Combust. Flame* 161 (4) (2014) 1048–1054.
[33] S.W. Huang, J.C. Lou, Y.C. Lin, Treatment of VOCs with molecular sieve catalysts in regenerative catalytic oxidizer, *J. Hazard. Mater.* 183 (1–3) (2010) 641–647.
[34] X.Z. He, F. Dong, W.G. Han, Z.C. Tang, Y. Ding, Recent advances and future challenges in the catalytic combustion of light hydrocarbon VOCs, *J. Mater. Chem. A* 12 (13) (2024) 7470–7507.
[35] J.C. Lou, S.W. Huang, Treatment of gaseous toluene using a regenerative catalytic oxidizer over supported copper oxide catalysts, *Environ. Eng. Sci.* 26 (3) (2009) 579–588.